

Optimal design of a three tape-spring hinge deployable space structure using an experimentally validated physics-based model

Hongling Ye¹ · Yang Zhang¹ · Qingsheng Yang¹ · Yanni Xiao² · Ramana V. Grandhi³ · Christopher C. Fischer³

Received: 10 February 2017 / Revised: 4 September 2017 / Accepted: 6 September 2017 / Published online: 18 September 2017
© Springer-Verlag GmbH Germany 2017

Abstract An optimal design approach is developed for a self-driven, self-locking tape-spring under a pure bending load in deployable space structures. A novel hinge with three tape springs is investigated and designed via an optimization process. Firstly, we investigate the steady-state moment and maximum stress of the hinge during deploying and folding processes using physics-based simulations. Experimental analyses are then conducted to verify the physics-based simulation results. Secondly, a parametric analysis is carried out to prove that both the tape spring thickness and subtended angle have significant effect on steady-state moment. A Response Surface Methodology (RSM) is employed to define an optimal surrogate model aimed at maximizing the steady-state moment, subjected to allowable stress. Finally, the Large Scale Generalized Reduced Gradient (LSGRG) optimization algorithm is used to solve the optimal design problem. Optimization results show that steady-state moment is increased by 19.5% while satisfying a maximum stress constraint. The proposed method is promising for designing novel deployable structures with high stability and reliability.

Keywords Tape-spring hinge · Deployable structure · Space structure · Driving ability

1 Introduction

A tape-spring is a thin-walled, open cylindrical structure with a natural curved cross-section used in deployable space structures. Carpenter's tape is the most similar physical example of a tape-spring. This advanced tape-spring can be elastically folded and automatically deployed through the release of stored energy, there are many advantages in comparison with conventional deployable structures adopting pin-joint connections. Moreover, the striking strengths of light weight, low cost, and friction insensitiveness make it popular for space applications. When the tape-spring encounters a coupling moment, the spring yields to the short axis (perpendicular to the length of the tape-spring), in which the mechanical responses, such as moment-rotation relationship and energy variation are nonlinear and direction dependent. As is shown in Fig. 1, if the direction of couple is opposite to the natural transverse curvature, the tape-spring produces a sudden snap-through buckling to form a reverse folding. In contrast, a more gradual positive folding is generated if the direction of couple is in the same direction as the transverse curvature (Seffen et al. 2000).

Analytical developments on tape springs linking the rotation angle and moment responses were first introduced by Wuest (1954) and Mansfield (1973). Recently, a classical shell model with large displacements and large rotations was defined via a dynamic physics-based simulation model, and the equation of steady-state moment for the tape-spring is given by theoretical derivation (Seffen et al. 2000; Seffen 2001; Guinot et al. 2012; Bourgeois et al. 2012). In addition, the folding is extended to the third-dimension and the relationships between moment responses, curvatures, as well as

✉ Hongling Ye
yehongl@bjut.edu.cn

✉ Ramana V. Grandhi
ramana.grandhi@wright.edu

¹ College of Mechanical Engineering and Applied Electronics Technology, Beijing University of Technology, Beijing 100124, China

² Beijing Satellite Manufacturing Factory, Beijing 100190, China

³ College of Mechanical and Materials Engineering, Wright State University, Dayton, OH 45435, USA

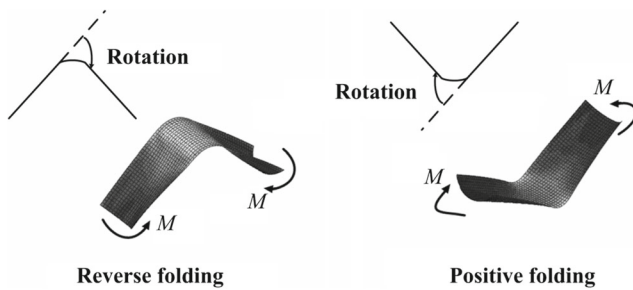


Fig. 1 Schematic diagrams of positive and reverse folding

torsion angle are predicted by using a variational approach (Walker and Aglietti 2004). The experimental set-up is designed to verify the analytical results of peak moment, steady-state moment, and torsional moment (Walker and Aglietti 2006).

After identifying the mechanical attributes of a tape-spring, the design of the tape-spring hinge consisting of two or more single tape springs was investigated. Two main forms of the tape-spring hinge are designed for deployable space structures. The first of which is the tube hinge (a tube with two or more cutting slots). The second deployable space structure design is a general tape-spring hinge (a hinge with two or more tape springs). The tube hinge, made of composite material, is constructed with two and three cutting slots, and moment responses are investigated theoretically and simulated based on experimentally verified physical models (Yee and Pellegrino 2005; Soykasap 2009; Mallikarachchi and Pellegrino 2011). Tape-spring hinges consist of differing layouts which result in various design diversity. Santer (2010) uses two tape springs and two straight strips to construct a bistable jumping hinge and gives the equations of motion, verified computationally and experimentally. Dewalque et al. (2016) utilized quasi-state analysis for a two paratactic tape spring layout to investigate moment and von Mises stress with respect to rotation. The three tape-spring hinge is examined to determine the maximum holding moment and minimum driving moment by Sicre and Givois, (2005). Additionally, the self-locking phenomenon is studied via quasi-static analysis along with torsional response within folding and deploying processes by Hoffait et al. (2010). The multi-body dynamics of a solar array driven by a three tape-spring hinge is explored alongside the kinematic equations for the solar panels by Kim and Park (2015). Deploying process moments with respect to deploying angle for these hinges are investigated by Sicre and Givois, (2005), Kim and Park (2015). Soykasap (2007) investigated the folding process moment of a four tape-spring hinge with a cross layout configuration computationally. It has been shown that tape-spring hinges have sufficient driving ability, and in fact the overshoot of a solar panel in a deploying process is likely and should be avoided to decrease the risk of vibration. Based on this, Ju et al. (2012) compared three kinds of tape-

spring hinge designs to decrease the overshoot using computational and experimental methods. The tape-spring hinge with dampened deployment is investigated experimentally and compared to simulated results by Dewalque et al. (2015).

Table 1 is given to illustrate the overview of the research for tape-spring hinges. It is shown that although a tape-spring structure is simple, geometric parameters and layouts result in drastic mechanical attribute differences. Therefore selecting optimal design of geometric parameters and layouts is essential to obtaining excellent mechanical attributes. Response Surface Methodology (RSM) (Hou et al. 2012 and 2014) is introduced to describe the explicit relationship between parameters and resultant mechanical attributes for this purpose. Yin et al. (2015) solved the equations related to this explicit relationship within proper constraints. Yang et al. (Yang et al. 2014 and 2015) optimized slot length and slot width of the double-layer tape-spring hinge on peak moment through multi-objective optimization with a modified Non-Dominated Sorting Genetic Algorithm (NSGA-II) based on RSM. Dewalque et al. (2016) investigated the geometric influence on tape-spring hinge mechanical attributes for reflector deployment, and presented an optimal procedure for minimizing the maximum stress and motion amplitude given in deploying scenarios.

This paper shows a novel optimization process for tape-spring hinge design. The mechanical attributes of a specially designed tape-spring hinge are investigated with numerical simulation that was validated by experimental results. Furthermore, the optimal model with maximum steady-state moment subject to an allowable stress limit is established. Based on the parametric analysis, the thickness and subtended angle of a given tape-spring are selected as design variables. RSM is used to define the explicit relationship between responses and design variables. The Large Scale Generalized Reduced Gradient (LSGRG) algorithm is employed to solve the optimization problem.

2 Physics-based simulation

2.1 Single tape-spring analysis

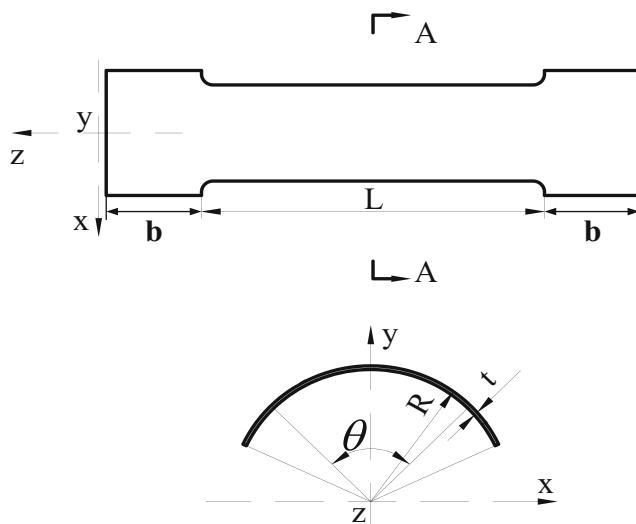
The geometry of a specially designed tape-spring is shown in Fig. 2. The cross section includes subtended angle θ , uniform thickness t , radius of curvature R , length L , and the two clamped ends with width b . These clamped ends are used to fix the tape-spring in folding and deploying mechanisms. The material properties of a steel alloy from which the tape-spring is constructed are $L = 120$ mm, $t = 0.15$ mm, $R = 18$ mm, $\theta = 90^\circ$, $b = 20$ mm, $E = 200$ GPa, and $\nu = 0.3$.

ABAQUS, a finite element analysis (FEA) software package, is used to model the tape-spring. An assumption is given

Table 1 Overview of previous research on tape-spring hinge

Forms	Researchers	Research objective	Main works (findings)
Tube hinge	Yee and Pellegrino 2005 Soykasap 2009	tube hinge	• structure: composite tubes with two and three slots
Tape-spring hinge	Mallikarachchi and Pellegrino 2011		• analytical expression given linking moment and curvatures
	Santer 2010	two tape springs	• new structural design
	Dewalque et al. 2016		• kinematic and mechanical attributes analysis
	Sicre and Givois 2005	three tape springs	• new structural design
	Hoffait et al. 2010		• driving and locking abilities determination using simulation and experiment
	Kim and Park 2015		• kinematic analysis for solar panels using tape spring hinge
	Soykasap 2007	others	• moment investigation of hinge with cross tape-spring layout
	Ju et al. 2012		
	Dewalque et al. 2015		• new structural design and damping introducing to weaken overshoot in deployment process

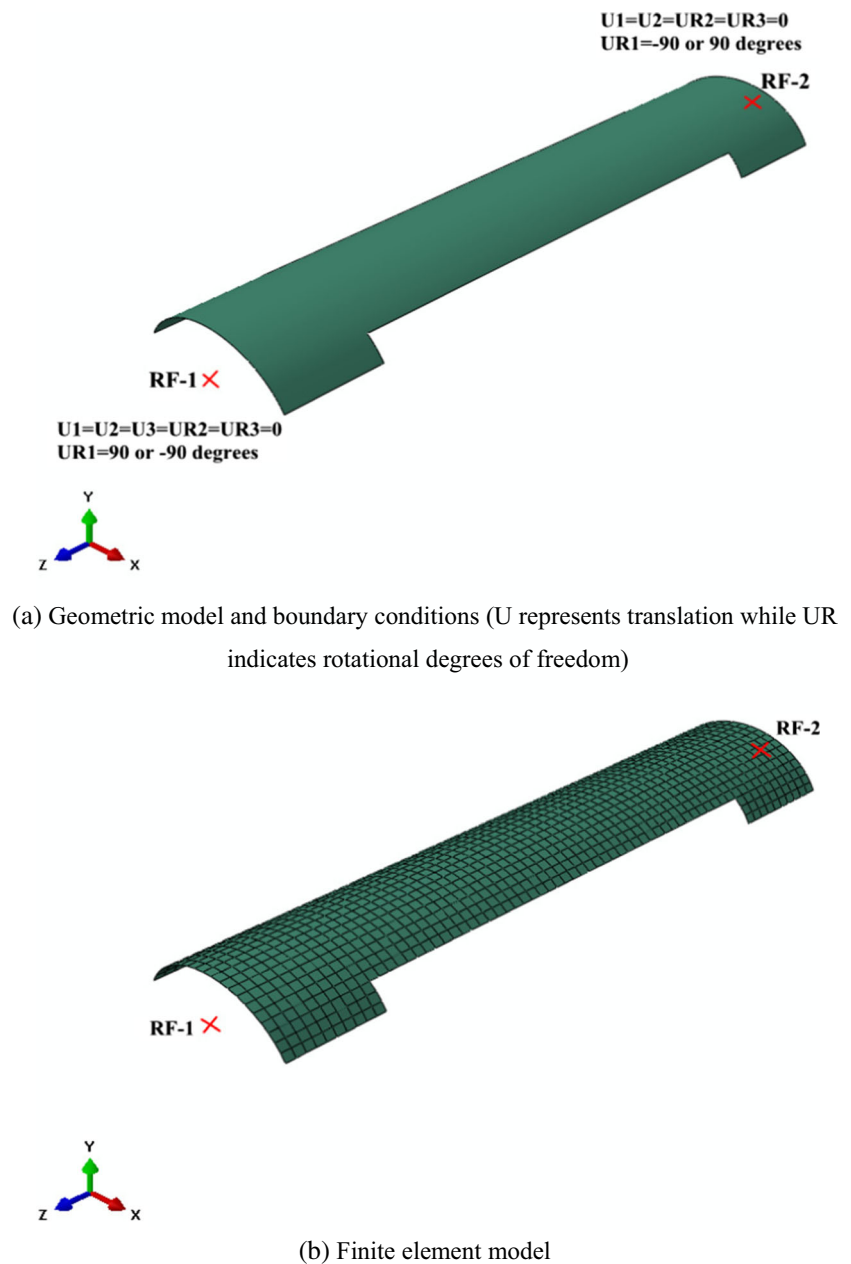
that a small-strain, large-displacement behaviour of the linearly elastic material exists in dynamic folding; therefore, a quadrilateral shell element with four corner nodes and five degrees of freedom (S4R5) at each node is selected to model the spring. To achieve pure bending, two reference nodes are established and connected to the edges of the tape-spring end cross-section through multi-point constraints (MPC), on which the specified equal (in magnitude) and opposite (in direction) angular displacements are applied. One of the reference nodes is permitted to rotate about the axis of bending, while the other is free to translate and rotate. These details are illustrated in Fig. 3. If reference node 1 (RF-1) is 90° and reference node 2 (RF-2) is -90° , the folding process is considered to be positive folding, thus if RF-1 and RF-2 have opposite rotations, this case is considered to be reverse folding. Starting from a fully folded configuration, the two reference nodes are given the opposite angular displacements

**Fig. 2** Geometry model of a tape-spring

discussed above and the tape spring will rotate back to its initial straight state, thus achieving the deploying process. Take positive folding for example, the folding process is achieved with RF-1 at a 90° rotation and RF-2 at a -90° rotation; whereas, the deploying process is achieved via setting RF-1 to -90° and RF-2 to 90° . It is worth noting that rotation angle is defined as the angle between two generatrices of the cylinder shell as seen in Fig. 1.

The commonly known process of folding and deploying of a tape-spring is given in Fig. 4 (inspired by Seffen et al. (2000)). Detailed descriptions and a simplified diagram are given by Seffen et al. (2000) in which the major features of moment variation were reviewed. For a tape-spring folded in a reverse sense, the moment variation increases linearly over a small rotation range, followed by a peak moment (M_+^{\max} , 1719.72 N.mm), and a vertical drop follows at this value of the moment due to buckling. Then the moment remains constant up to a fully folded state and is theoretically equal to the steady moment (M_+^* , 153.03 N.mm). During deploying, the moment follows almost the same path of folding but snaps back at smaller rotations associated to buckling. The inconsistency between folding and deploying is responsible for hysteresis phenomenon resulting in self-locking of a hinge in the straight configuration. As for a positive sense, asymmetrically local deformations move along the tape-spring and then induces symmetric folding at the end. The moment response in this folding process is similarly characterized using peak moment (M_-^{\max} , 1436.31 N.mm) and an approximately steady moment (M_-^* , 83.80 N.mm). However, for positive deploying, it is commonly assumed that the deploying path is superimposed on the folding state (Dewalque et al., 2016), while the moment evolution snaps back at the same rotation with a reduced peak moment. It is shown that local deformation results in torsion; therefore, the peak moment in folding is fluctuant and higher than that in deploying processes as

Fig. 3 Tape-spring representation



(a) Geometric model and boundary conditions (U represents translation while UR indicates rotational degrees of freedom)

(b) Finite element model

depicted in Fig. 4. Apparently the steady-state moments in a deploying process are equal to the values observed in the folding process, and the corresponding processes are relatively stable. Therefore, we only focus our attention on the steady-state moment variation in the deploying process.

2.2 Three tape-spring hinge analysis

Compared with a single tape-spring hinge, a three tape-spring hinge possesses a smooth stress distribution and improves the moment to guarantee stability of the deployable structure. Therefore, the mechanical attributes of a three tape-spring hinge are explored in this work. This hinge is constructed with two tape-springs set side-by-side,

with a third set in the opposite direction between the first two as shown in Fig. 5. The main parameters include the horizontal distance between the centroid of the spring cross-sections, recorded as $hl = 32.4$ mm, and the vertical distance, recorded as $sl = 16$ mm.

The quasi-static method with ABAQUS/Explicit solver is used to solve highly nonlinear problems, as is the case in this three tape-spring hinge. Considering the small strain, warping, and deformation of a tape-spring due to high nonlinearity, the tape-springs are meshed with S4RSW shell elements. Two reference nodes are set at each cross-sectional centroid and connected to the rigid ends of the hinge using Tie constraints. Degrees of freedom are the same as those discussed in the previous section on single tape-spring hinges. The geometric

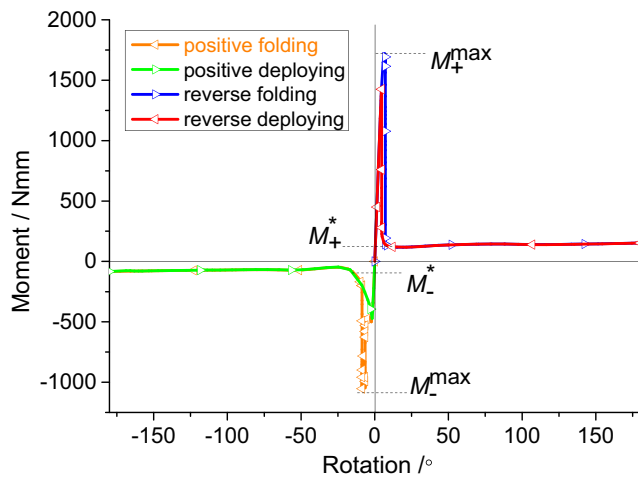


Fig. 4 Moment-rotation relationships of single tape-spring hinge

and FEA models are shown in Fig. 6. To dissipate the kinetic energy produced in the quasi-static folding, the simulation must run for 100 s to ensure the hinge stabilizes. Following the physics-based simulation, the fully folded configuration and stress distribution contour of the three tape-spring hinge are obtained and given in Fig. 7. It is shown that the maximum stress is distributed throughout the folded region of the reverse tape spring. From this fully folded state, a quasi-static simulation of the three tape-spring hinge deploying process can be achieved by adopting the degree of freedom settings discussed in Section 2.1.

Energy variations have been plotted in Fig. 8. The strain energy profile is mostly symmetric with two spikes during folding at a rotation of 0.94° and 25° , respectively. It is observed that the snap-through buckling of the reverse folding tape spring leads to the first spike in the folding process, while the second spike is a result of local deformation of the positive folding tape-spring. The spikes do not appear at the same rotation within the deploying process. Strain energy decreases almost linearly until the rotation angle reaches 10° , at this point the transition corresponds to the hinge snapping back. Then, strain energy declines at a considerably faster rate until it is fully deployed. The non-zero strain energy of the hinge is obtained to indicate that the structure has small permanent deformation. Since the amplitudes of these three kinds of energy are not at the same magnitude, the characteristics of kinetic energy and energy balance with respect to rotation are not

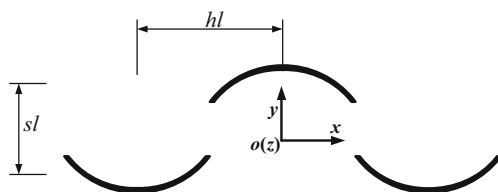


Fig. 5 Layout of three tape-spring hinge

obvious as shown in Fig. 8. Therefore these values are enlarged to observe the changing of the kinetic energy and energy balance through the entire process. It is shown from the curve being enlarged that the kinetic energy remains approximately zero, with the exception of two jumps corresponding to spikes of strain energy at respective rotations. Energy balance increases slowly to a small value, then it jumps to a relatively high value and remains constant until the hinge fully deploys. The energy balance remains fairly constant throughout the folding and deploying simulation cycle. In addition, the kinetic energy is negligible compared to strain energy, which indicates that the response is quasi-static, implying that the results are accurate. On the other hand, the energy variations in a deploying process are more stable than in a folding process; therefore the investigation is performed on the deploying process.

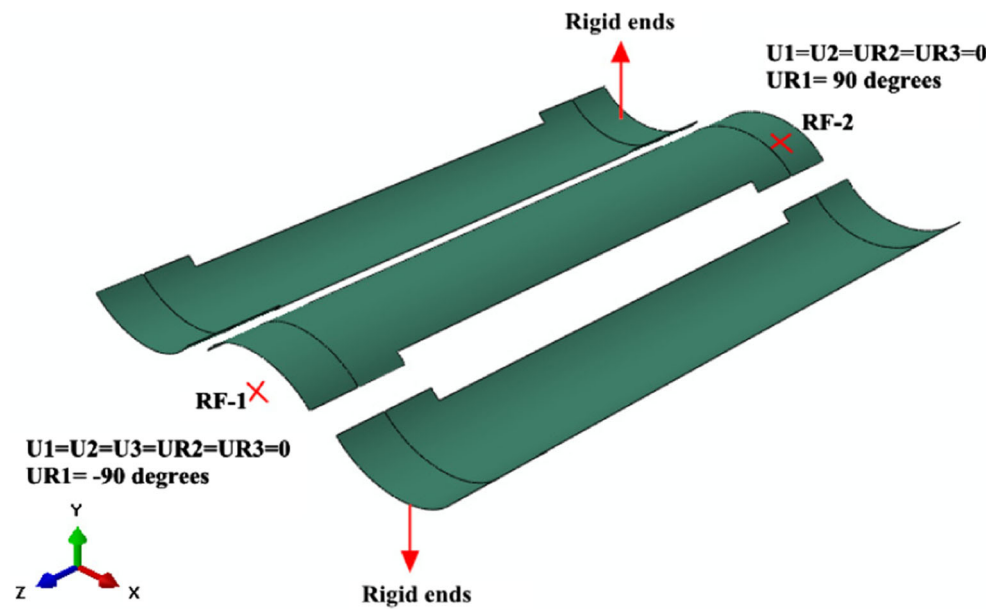
Comparisons between moments obtained computationally and experimentally are shown in Fig. 9. The moment observed computationally grows to a peak and then snaps back to a smaller value followed by an approximate constant $238.7 \text{ N}\cdot\text{mm}$ until the folding is completed. The peak corresponding to the buckling of the opposite tape spring in the hinge has a value of $14,847.7 \text{ N}\cdot\text{mm}$. For a deploying simulation, its moment follows a very similar path as the folding process. However, in this case moment has no snap back to the originally straight state and appears due to some permanent deformation of the tape-spring. This can also be found in energy curves with residual strain energy. In light of these results, the experiment is essential to the development of an accurate finite element model. An experimental set-up can be seen in a publication by Ye et al. (2017). Note that from full folding, the experimental moment remains constant up to a rotation of 10° , after which the moment can't be recorded due to the fast snap speed. In addition, the observed steady moment is $232.1 \text{ N}\cdot\text{mm}$, which is less than that observed through simulation due to the friction between the guide rails.

From the results of Section 2.1, the simple superposition of one reverse bending tape-spring and two positive bending tape-spring produces a critical moment of $4592.34 \text{ N}\cdot\text{mm}$ and a steady-state moment of $320.63 \text{ N}\cdot\text{mm}$. It is obvious that the critical moment and steady-state moment of a three tape-spring hinge are not equal to the simple addition of single tape-spring hinges.

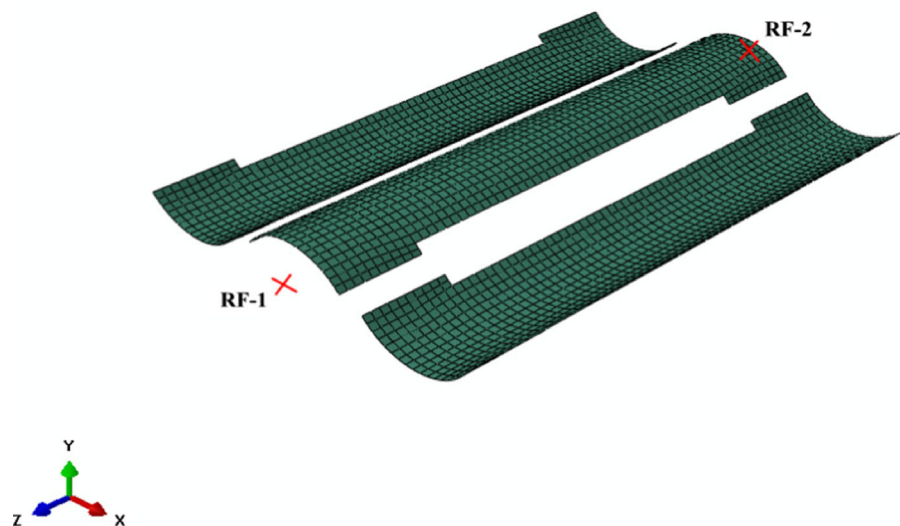
3 Experimental validation

To validate the finite element models described earlier in this work, experiments were conducted on a three tape-spring hinge. The experimental apparatus consists of an active driving shaft fixed to a rigid base and a passive driving shaft

Fig. 6 Three tape-spring hinge representation



(a) Boundary conditions of three tape-spring hinge



(b) Finite element model of three tape-spring hinge

mounted on a slide way. The drive shaft limits all rotational degrees of freedom in order to achieve pure bending. The slide way provides a way to guide the horizontal motion of the tape-spring during folding.

The deployed deformation shapes obtained through both experiment and simulation, are compared in Fig. 10 in 10° intervals of rotation. At each interval, the maximum stress of the hinge is observed. This maximum stress will be used later to constrain the optimization problem. Comparison of results shows that the experimental and physics-based simulation results have good agreement for a deployment step, thus ensuring accuracy of the computer simulations.

4 Parametric analysis

The steady-state moment is regarded as one of the important characteristics in measuring the driving ability of a deployable hinge. To better comprehend the steady-state moment variation with geometric parameters, the effects of length, radius, subtended angle, and thickness on the moment of a three tape-spring hinge are explored prior to optimization. As discussed, the excessive stress caused by the high nonlinearity in dynamic folding and deploying steps of a three tape-spring hinge may result in permanent deformation, as can be seen from the energy profile in Fig. 8. Therefore, the maximum stress corresponding to each design is also investigated.

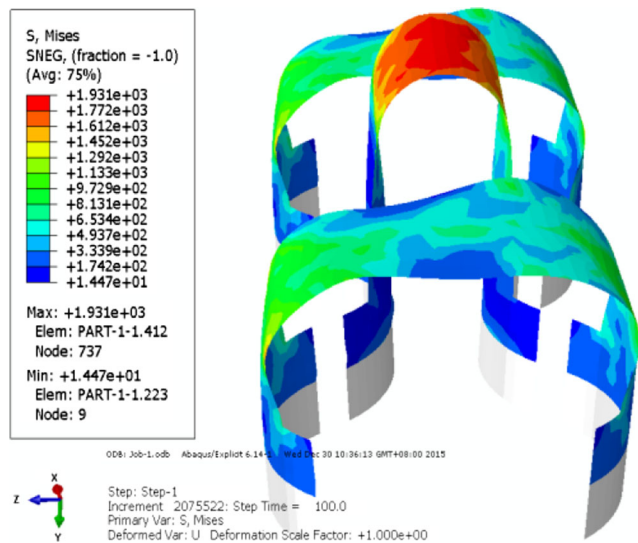


Fig. 7 Stress distribution contour of fully folded three tape-spring hinge (with single tape-spring design of $L = 90$ mm, $R = 18$ mm, $t = 0.15$ mm, $\theta = 90^\circ$)

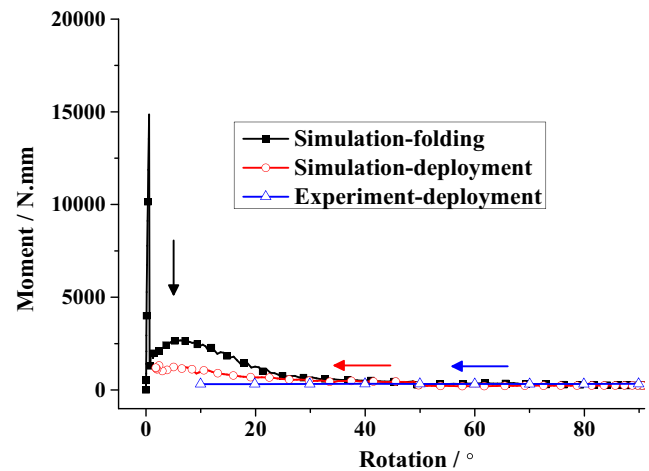
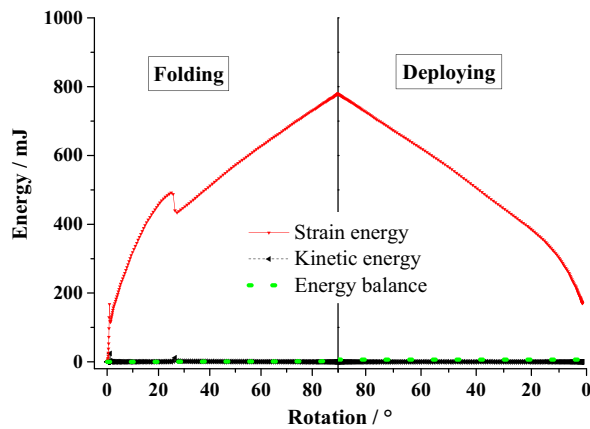
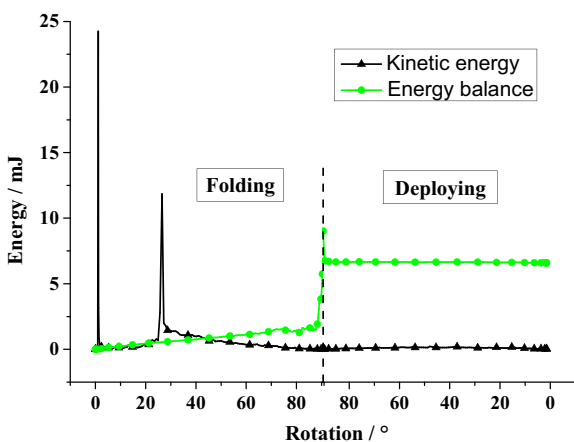


Fig. 9 Moment variations of three tape-spring hinge



(a) Energy in folding and deploying processes



(b) Enlarged plot for kinematic energy and energy balance

Fig. 8 Energy variation curves

4.1 Length variation

The length of a single tape-spring with design parameters $t = 0.15$ mm, $R = 18$ mm, and $\theta = 90^\circ$ was varied from 80 mm to 130 mm. The effects of length on mechanical attributes of the hinge were simulated. Therefore the moments and maximum von Mises stress were obtained with differing lengths, as given in Table 2. It can be seen that an increase in length corresponds to a decrease in critical moment. Note that the maximum von Mises stress behaves as a linear decrease with increasing length, except for $L = 130$ mm. For this case, local deformations of two positive tape springs occur, resulting in the nonlinearity of stress. As for the steady-state moment, the variation shows a nonlinear tendency to increase first and then drop with a little fluctuation for case $L = 100$ mm. To understand how the steady-state moment varies with length in a folding and deploying cycle of the hinge, variation curves are drawn in Fig. 11.

4.2 Thickness variation

In the context of thickness varying from 0.10 to 0.20 mm with design parameters $\theta = 90^\circ$, $R = 18$ mm, and $L = 90$ mm, the effects of thickness on mechanical attributes of the hinge are obtained and presented in Table 3. From the values in the table, the critical moment is greatly increased with an increase in thickness. It can be seen that the steady-state moment and maximum von Mises stress have approximately the same linear increase with increase in thickness. Similarly, the profiles of the moment with respect to thickness in a folding and deploying cycle of the hinge are drawn in Fig. 12. From the moment variation curves in Fig. 12, it should be noted that there is a small permanent deformation caused by excessive local stress; therefore, it is not acceptable to allow stress to increase beyond a safe limit.

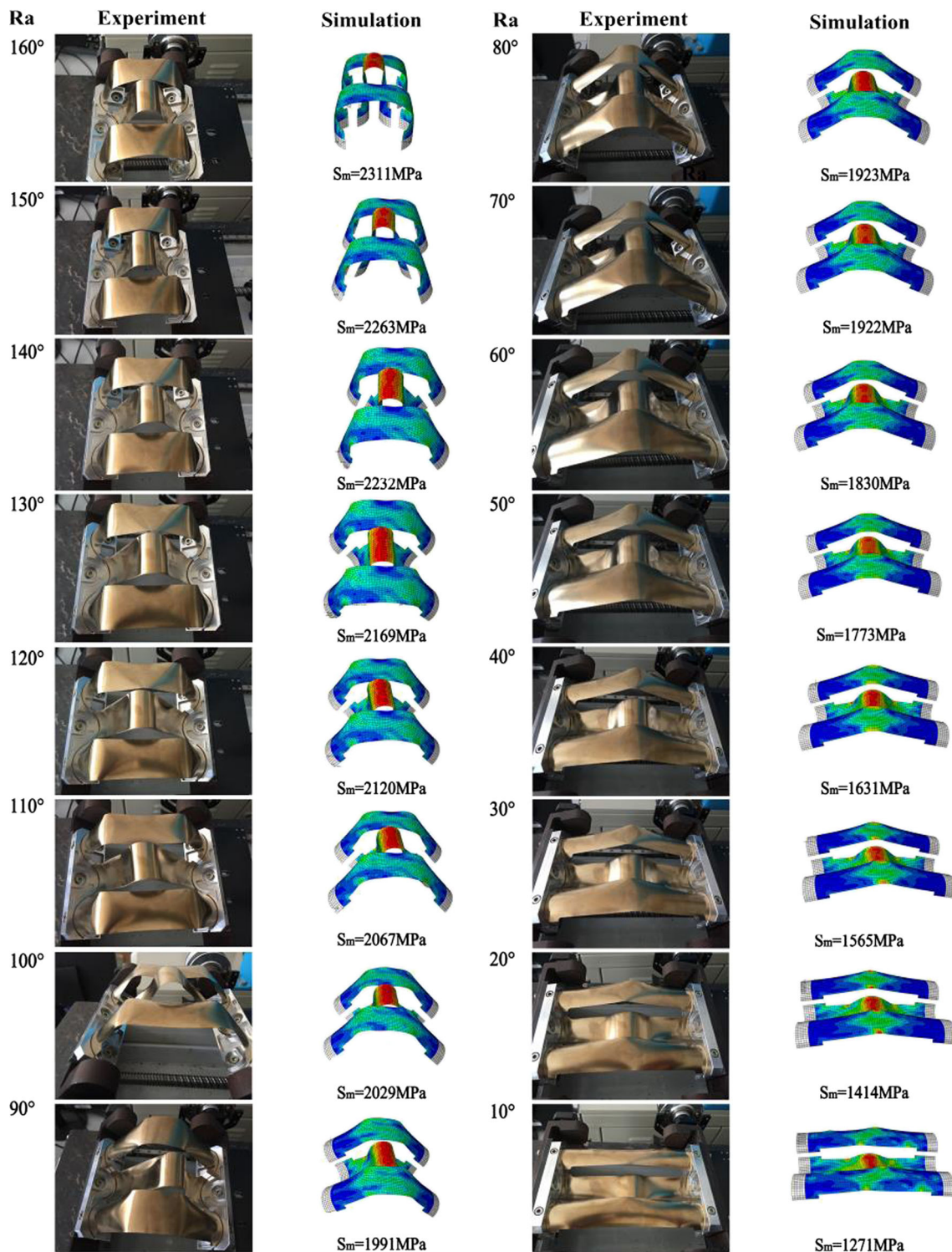


Fig. 10 Configuration comparisons of numerical simulation and experiment (Ra represents rotation angle, Sm indicates maximum von Mises stress. Three tape-spring hinge is designed with single tape-spring design of $L = 120$ mm, $R = 18$ mm, $\theta = 90^\circ$, $t = 0.15$ mm)

4.3 Subtended angle variation

The subtended angle effect analysis was performed by varying the subtended angle from 50° to 100° while holding $t = 0.15$ mm, $L = 90$ mm, and $R = 18$ mm constant. The

parametric analysis results are given in Table 4. Similarly, the variation curves for moment with respect to subtended angle in a folding and deploying cycle of the hinge are drawn in Fig. 13. It can be seen in Table 3 that increasing the subtended angle results in a significant increase of the

Table 2 Moment values for different lengths

L	Steady-state moment	Critical moment	Max. von Mises stress
mm	N.mm	N.mm	MPa
80	164.2	18,662.2	2326.5
90	290.2	17,672.9	2004.9
100	237.4	16,320.8	1779.4
110	300.8	15,160.5	1732.9
120	238.7	14,847.7	1204.4
130	148.7	13,848.4	1690.9

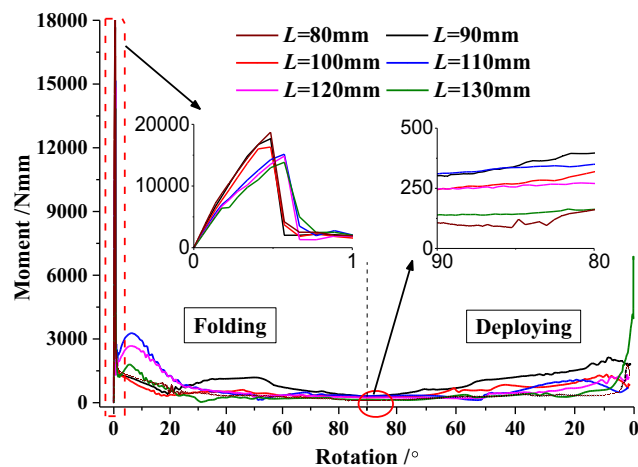
Table 3 Moment values for different thicknesses

t	Steady-state moment	Critical moment	Max. von Mises stress
mm	N.mm	N.mm	MPa
0.10	36.9	1847.0	1433.6
0.12	133.3	13,279.6	1598.7
0.14	229.0	14,927.0	1911.7
0.16	346.97	18,651.2	2195.6
0.18	425.2	23,110.2	2288.5
0.20	620.9	26,767.3	2489.93

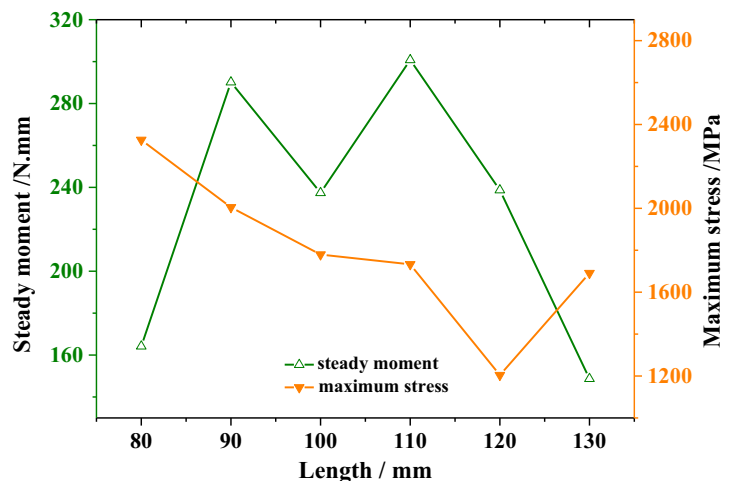
critical moment. It is interesting to observe that the steady-state moment and maximum von Mises stress behave comparably to each other. However, a subtended angle of 90° shows a higher value of steady moment. Similarly, the two positive folding tape springs have localised torsional deformations leading to the increase of moment. On the other

hand, from moment analysis in section 2.2, the steady moment of a three tape-spring hinge is not equal to the simple superposition of single tape spring, this implies the steady moment in a three tape-spring hinge shows a nonlinearity. Therefore, the subtended angle of 90° exhibits a higher steady moment.

Fig. 11 Parametric analysis of length

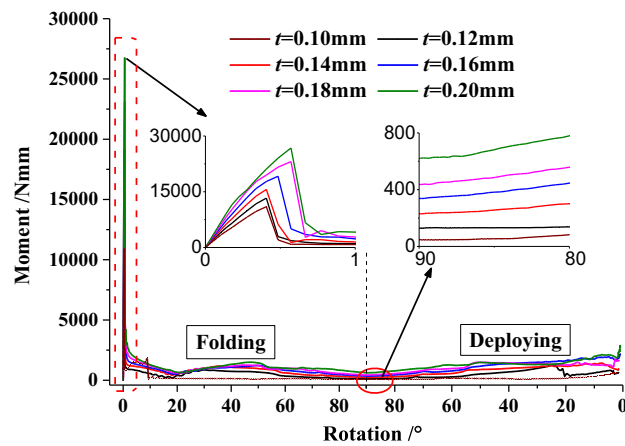


(a) Variation of moment for different lengths

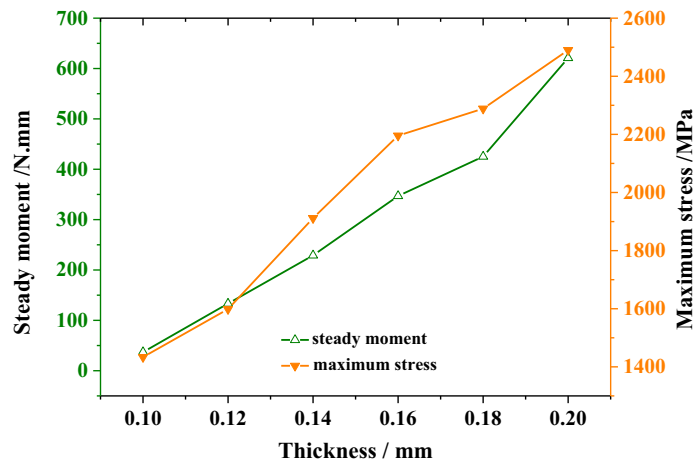


(b) Variation tendencies of steady moment and stress for different lengths

Fig. 12 Parametric analysis of thickness



(a) Variation of moment for different thicknesses



(b) Variation tendencies of steady moment and stress for different thicknesses

4.4 Radius variation

The parametric analysis is carried out with $t = 0.15 \text{ mm}$, $L = 90 \text{ mm}$, and $\theta = 90^\circ$ while R is varied from 12 mm to 22 mm. These effects are given in Table 5. As in the

Table 4 Moment values for different subtended angles

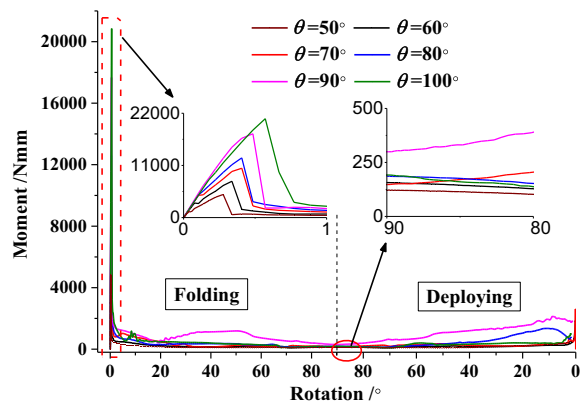
θ	Steady-state moment	Critical moment	Max. von Mises stress
°	N.mm	N.mm	MPa
50	124.2	4870.9	1671.7
60	157.5	7659.8	1741.6
70	140.1	10,408.6	1499.1
80	183.2	12,593.0	1833.6
90	290.2	17,672.9	2004.9
100	190.3	20,849.3	1707.7

previous sections, the variation profiles of moment with respect to radius in a folding and deploying cycle of the hinge are drawn in Fig. 14. These results show that critical moment has a monotone linear relationship with radius, where an increase in radius results in an increase in critical moment. Steady-state moment results show a significantly irregular variation with respect to radius, which means that the steady-state moment is relatively sensitive to a change in radius. However, maximum stress tends to increase with the radius, with the exception of a slight drop between radius of 14 mm and 18 mm.

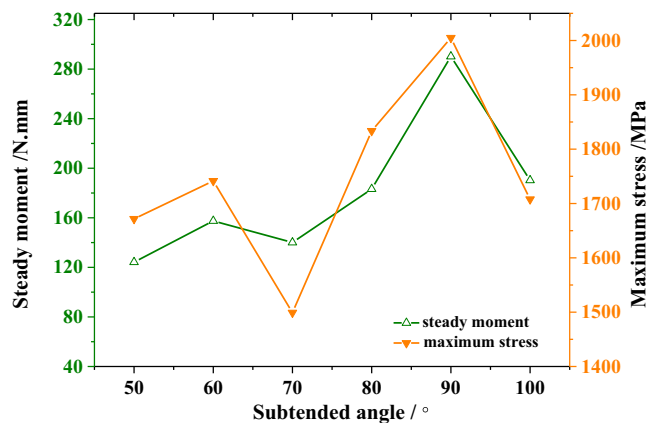
4.5 Primary and secondary sequence analysis

To better understand parameter effects on performance of the hinge, a primary and secondary sequence analysis was carried out. According to the literature (Wang and Sui 2012), in the multiple linear regression equation, the partial regression coefficients b_1, b_2, \dots, b_{m-1} indicate the

Fig. 13 Parametric analysis of subtended angle



(a) Variation of moment for different subtended angles



(b) Variation tendencies of steady moment and stress for different subtended angles

specific effects of x_i on y . However, the general case $b_j (j = 1, 2, \dots, m - 1)$ does not directly reflect the relative importance of these independent variables. This is because the value of b_j is affected by the factor value. This issue can be resolved by standardizing the partial regression coefficient b_j .

Assuming that the standardized coefficient of partial regression coefficient b_j is $P_j (j = 1, 2, \dots, m - 1)$, where P_j is given by (1), and $L_{jj} = \sum_{i=1}^n (x_{ji} - \bar{x}_j)^2$ and $L_{yy} = \sum_{i=1}^n (y_i - \bar{y})^2$.

According to the standard regression coefficient P_j value, the significance of each factor (independent variable) x_i to the response y can be directly determined. The greater the P_j , the more important the corresponding factor becomes:

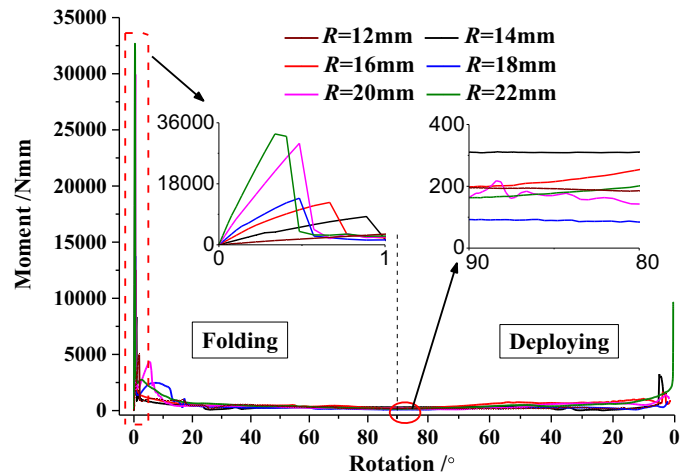
$$P_j = |b_j| \sqrt{\frac{L_{jj}}{L_{yy}}} \tag{1}$$

Using this theory, a sequence analysis was carried out with four factors, each having two levels. The responses, steady-state moment and maximum von Mises stress, were obtained and given in Table 6. Taking $x_1 = R, x_2 = t, x_3 = \theta, x_4 = L$, the standardized coefficients and influence ranks are shown in Table 7. It can be seen from the table that the top two influence factors for steady moment are thickness and subtended angle; as for stress two significant influence factors are thickness and radius. While the influences of radius and subtended angle as well as length on stress are at the same level, from a comprehensive comparison, the two parameters thickness and subtended angle are selected as design variables for optimization.

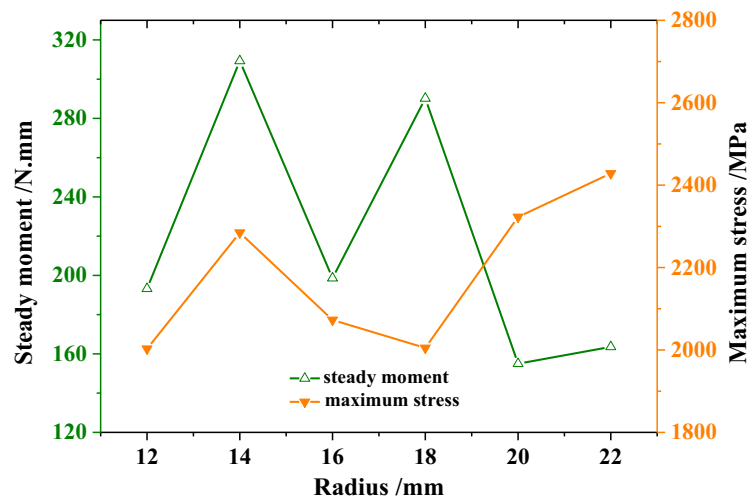
Table 5 Moment values for different radii

R	Steady-state moment	Critical moment	Max. von Mises stress
mm	N.mm	N.mm	MPa
12	193.2	5041.5	2003.0
14	309.3	8339.3	2284.6
16	198.6	12,511.2	2072.9
18	290.2	17,672.9	2004.9
20	155.0	29,942.4	2322.8
22	163.6	32,709.0	2428.3

Fig. 14 Parametric analysis of radius



(a) Variation of moment for different radii



(b) Variation tendencies of steady moment and stress for different radii

5 Optimization investigations

5.1 Optimization model for three tape-spring hinge

The optimization problem is to maximize the steady-state moment subject to a constraint on maximum stress. Smooth deployment of the hinge is an extremely important measure for the completion of the space mission. Excessive stress would cause damage to the tape-spring and hinder deploying performance of the hinge. Therefore, maximum stress must remain below the allowable stress dictated by the steel alloy material used to construct the hinge; thus, maximum stress is taken to be a constraint on the optimization problem. As discussed previously in this paper, the steady-state moment is a significant characteristic for measuring the drivability of the hinge; thus, steady-state moment is selected as the objective. From the primary and secondary sequence analysis, thickness and subtended angle were deemed most influential to steady-state

moment and thus used as design variables. The final optimization problem for a three tape-spring hinge is mathematically represented by (2):

$$\begin{cases} \text{Maximize : } M_s \\ \text{Subject To : } \sigma_{\max} \leq \bar{\sigma} \\ \underline{x}_i \leq x_i \leq \bar{x}_i \quad (i = 1, \dots, n) \end{cases} \quad (2)$$

where M_s is the optimization objective, the steady-state moment of the hinge in the folding process; σ_{\max} is the maximum von Mises stress of the hinge in the folding process; $\bar{x}_i, \underline{x}_i$ are the upper and lower bounds of the design variables, respectively; and n is the total number of design variables.

5.2 Response surface methodology (RSM)

Response Surface Methodology (RSM), used to obtain the relationship between the input and output of complex systems, is

a collection of mathematical and statistical techniques (Box and Wilson 1951; Sui and Yu 2011) and applied widely in engineering optimization process (Liu and Day 2008; Li et al. 2011 and 2013; Qi et al. 2012; Guo et al. 2013). In this paper, RSM is utilized to construct an inexpensive representation of the objective and constraint functions. The basic idea is to construct an explicit polynomial expression to represent the implicit function of the independent variables.

An RSM model is constructed on design variable t ranging from 0.1 mm to 0.2 mm and θ ranging from 60° to 90° . 25 sample points are collected using two five-level factors and the steady-state moment and von Mises stress responses are evaluated using the experimentally validated simulation.

The fourth-order polynomial function for steady-state moment is fitted using MATLAB and given in (3):

$$M_s(t, \theta) = 2.499 \cdot 10^6 t^4 - 0.004088 \theta^4 + 0.2005 t \theta^3 + 67.50 t^2 \theta^2 + 1.641 \cdot 10^4 t^3 \theta + 1.189 \theta^3 - 56.69 t \theta^2 - 1.779 \cdot 10^4 t^2 \theta - 2.766 \cdot 10^6 t^3 - 128.1 \theta^2 + 6.315 \cdot 10^3 t \theta + 1.31 \cdot 10^6 t^2 - 2.73 \cdot 10^5 t + 5.992 \cdot 10^3 \theta - 9.997 \cdot 10^4 \tag{3}$$

The same method is used to obtain the polynomial function for maximum von Mises stress given in (4):

$$\sigma_{\max}(t, \theta) = 1.49 \cdot 10^7 t^4 - 0.001127 \theta^4 - 1.305 t \theta^3 + 24.61 t^2 \theta^2 - 7.484 \cdot 10^4 t^3 \theta + 0.4819 \theta^3 + 2.891 \cdot 10^2 t \theta^2 + 2.977 \cdot 10^4 t^2 \theta - 3.527 \cdot 10^6 t^3 - 69.77 \theta^2 - 2.591 \cdot 10^4 t \theta - 2.880 \cdot 10^5 t^2 + 6.703 \cdot 10^5 t + 4.439 \cdot 10^3 \theta - 1.000 \cdot 10^5 \tag{4}$$

The original 25 sample point designs are substituted into the above two RSM models to obtain the function values of steady-state moment and maximum von Mises stress yielding an RSME for objective function of 0.00362 and constraint function of 0.00019, respectively. It can be seen that the absolute value of the maximum relative error between the steady-state moment prediction and simulation result is no

more than 8%. Likewise, that of maximum von Mises stress is no more than 5%.

To evaluate the accuracy of the fitted functions, the complex correlation coefficient (R^2) and the modified complex correlation coefficient (R_{adj}^2) are introduced in (5 and 6). The fitted function is deemed more accurate when each coefficient is closer to a value of one. Another index for evaluating the accuracy of the fitted function is root mean squared error (RMSE) as seen in (7). An RMSE of zero indicates a perfectly fitted function. Related derivation and proofs are shown in the literature (Sui and Yu 2011).

Table 6 Test points and responses

No.	R mm	t mm	θ °	L mm	von Mises stress MPa	Steady-state moment N.mm
1	11	0.075	45	68	1165.6	10.86
2	11	0.075	75	68	1137.3	21.59
3	11	0.125	45	68	1889.2	38.99
4	11	0.125	75	68	1796.7	80.79
5	18	0.075	45	68	1407.7	87.95
6	18	0.075	75	68	1572.8	23.14
7	18	0.125	45	68	2349.0	58.38
8	18	0.125	75	68	2327.7	92.50
9	11	0.075	45	113	1133.2	10.51
10	11	0.075	75	113	1128.0	25.36
11	11	0.125	45	113	1979.8	34.61
12	11	0.125	75	113	1766.3	144.69
13	18	0.075	45	113	1741.68	13.41
14	18	0.075	75	113	1848.09	27.05
15	18	0.125	45	113	1217.6	49.76
16	18	0.125	75	113	1271.8	118.75

$$R^2 = 1 - \frac{\sum_{i=1}^m (y_i - \bar{y}_i)^2}{\sum_{i=1}^m (y_i - \bar{y})^2} \tag{5}$$

$$R_{adj}^2 = 1 - \frac{m-1}{m-N} (1-R^2) \tag{6}$$

$$RMSE = \left(\frac{\sum_{i=1}^m (y_i - \bar{y}_i)^2}{(m-p-1)} \right)^{0.5} \tag{7}$$

Table 7 Standardized coefficient of partial regression

Parameters	$P_f(\text{moment})$	Ranking (moment)	$P_f(\text{stress})$	Ranking (stress)
R	0.1599	3	0.2293	2
t	0.6157	1	0.4561	1
θ	0.3543	2	0.2038	4
L	0.0153	4	0.2176	3

where y_i is the FEA results of the i th sample point, \tilde{y}_i is the response of the i th sample point, and \bar{y} is the mean response of $y_i, i = 1, 2, \dots, m$, m is the number of design points, p is the number of non-constant terms in the response functions, and n is the number of the basic functions.

The complex correlation coefficient (R^2) of the steady-state moment response surface model and modified complex correlation coefficient (R_{adj}^2) are 0.99745 and 0.99734, respectively. Likewise, the complex correlation coefficient (R^2) and modified complex correlation coefficient (R_{adj}^2) for the maximum stress response surface model are 0.99232 and 0.99199, respectively. The values of RMSE for steady-state moment and maximum stress are 0.00362 and 0.00019, respectively. These three accuracy indicators suggest highly accurate fitted functions. Thus the accuracy of the two response surface models is satisfied.

By adding extra test points, different from the original 25 samples, the fitted response surface models are verified. From these tables, it can be seen that the absolute value of maximum relative error from steady-state moment function is less than 7%. Similarly, that of maximum von Mises stress is no more than 5%. The accuracy of these two response surface models is satisfactory, indicating that the explicit expression of the fourth-order response surface fitting can accurately express the relationship between simulation response and design variables.

5.3 Optimal solution

The Large Scale Generalized Reduced Gradient (LSGRG) algorithm, which can handle an optimization model with equality and inequality constraints, is used to solve the optimization problem. This optimization algorithm uses the following design space for design variables $t = [0.1, 0.2]$ and $\theta = [60^\circ, 90^\circ]$, with an initial design point of $x = [0.15, 75.0]^\top$. In order to ensure the safety of the structure in a folding process, it is crucial that the maximum von Mises stress of the tape-spring be less than the allowable stress of 2000 MPa. The required configurations of the LSGRG algorithm, that is, convergence epsilon and convergence iterations, are taken to be default values of 0.001 and 3, respectively. The optimal design is obtained after 97 iterations.

The optimal design obtained is $x = [0.132, 86.46]^\top$, that is, the thickness of the tape-spring is 0.132 mm and the subtended angle of its cross section is 86.46° . Table 8 shows the comparison of initial and optimal design points. The optimal steady-state moment increases from 145.5 N.mm to 173.94 N.mm, increasing by around 19.5%. The maximum stress increases from 1969.1 MPa to 2000.0 MPa, which satisfies the maximum allowable stress constraint.

Table 8 Comparisons between the original and optimal designs evaluated using RSM models

Items	θ	t mm	Steady-state moment N.mm	Max. von Mises stress MPa
Initial design	75	0.150	145.5	1969.1
Optimal design	86.46	0.132	173.94	2000
Variation	15.3%	12%	19.5%	1.6%

In order to verify the effectiveness of the algorithm using RSM models, the optimal design point is remodelled using the physics-based simulation model. Simulation and fitted function results are 158.47 N.mm and 173.94 N.mm for steady-state moment, respectively. Maximum von Mises stress results for simulation and fitted function are 1768 and 2000 MPa, respectively. The results of the fitted models seem to differ slightly from the simulation results, thus indicating additional simulations would help. Figs. 7 and 15 give the initial and optimal stress distributions of the three tape-spring hinge, respectively. Comparison of the results shows that the optimal design stress distribution is more uniform.

On the other hand, the optimal design is compared with the parametric study in section 4. According to the analysis of parametric influence, thickness and subtended angle are selected as the top two influential factors. Thickness and subtended angle are confined to $t \in [0.1, 0.2]$ and $\theta \in [60^\circ, 90^\circ]$. Maximum stress is constrained to be less than a yield point of 2000 MPa. As a new hinge needs at least 150 N.mm of steady moment to exert its driving ability, we consider the design within the above constraints. The parametric analysis was conducted by changing one of the two influential factors while keeping the other parameters fixed.

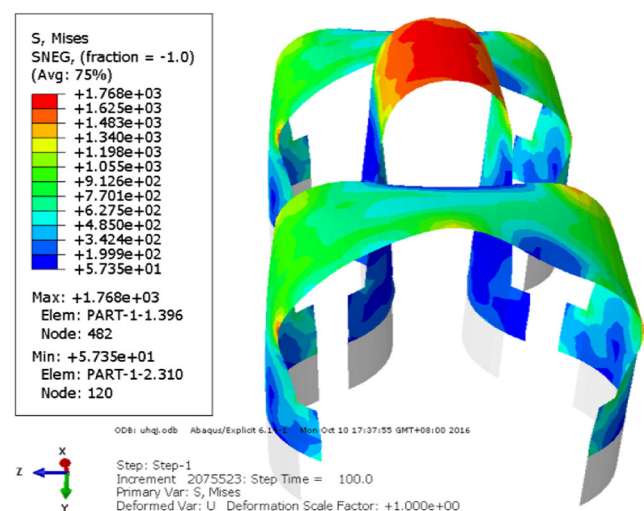


Fig. 15 Von Mises stress distribution of optimal design

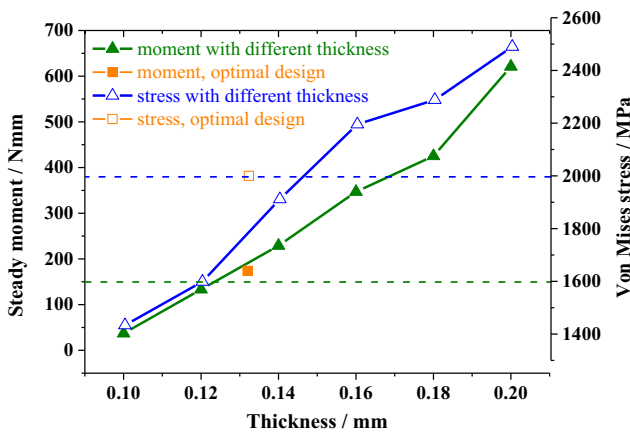


Fig. 16 Thickness comparisons between parametric study and optimal design

5.3.1 Case one, parametric study on thickness within $\in [0.1, 0.2]$:

The influence of thickness from Table 3 is visualized in Fig. 16. Two orange symbols indicate the optimal design results and it is shown that the region below the blue dashed line (representing constraint of stress below 2000 MPa) and above the green dashed line (representing minimum steady moment of 150 N.mm) is the feasible area satisfying all conditions.

5.3.2 Case two, parametric study on subtended angle with $\theta \in [60^\circ, 90^\circ]$:

The influence of subtended angle is also visualized in Fig. 17. The region below the pink dashed line (representing stress constraint below 2000 MPa) and above the black dashed line (representing minimum steady moment of 150 N.mm) and $\theta \in [60^\circ, 90^\circ]$ is the feasible area satisfying all conditions. A green circle and triangle indicate the optimal design results.

This optimal design process is summarized in the flowchart shown in Fig. 18.

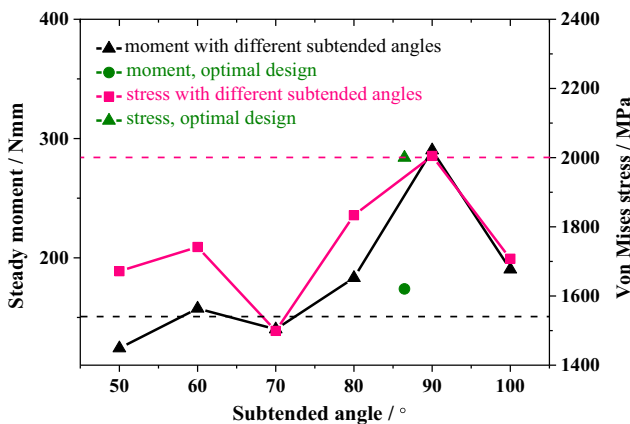


Fig. 17 Subtended angle comparisons between parametric study and optimal design

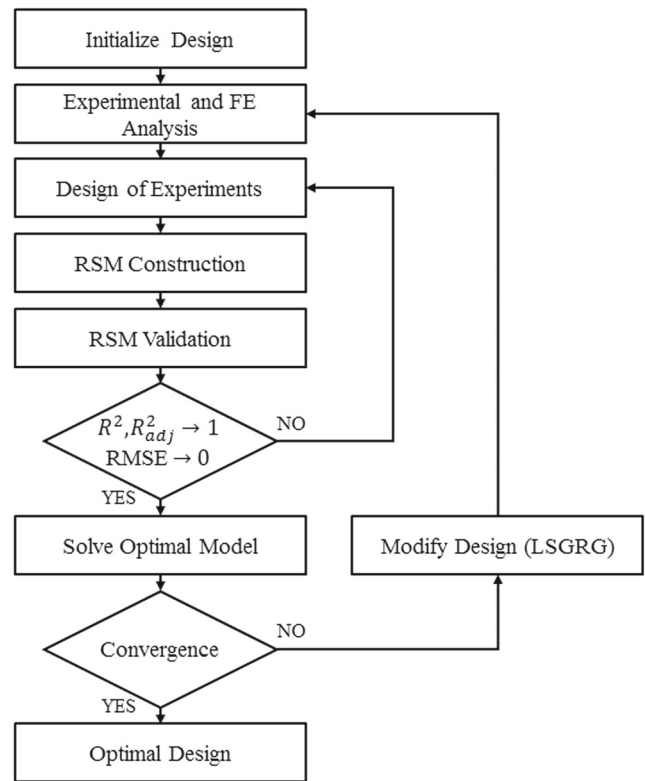


Fig. 18 Optimal program flowchart of three tape-spring hinge

6 Conclusions

This paper presented a detailed investigation on the folding and deploying processes of a single tape-spring hinge and a three tape-spring hinge. A three tape-spring hinge is optimally designed. The physics-based simulation method is employed to construct the geometric and finite element models for single tape-spring and three tape-spring hinges. The steady-state moment is deemed a significant characteristic for measuring driving ability of the hinge, so the steady-state moment variations of a single tape-spring hinge in positive and reverse folding are investigated through ABAQUS. The combination of three tape-spring is arranged to form a novel tape-spring hinge. Due to highly nonlinear relationships existing in the folding and deploying processes of a three tape-spring hinge, the quasi-static algorithm is applied in the simulation process. At the same time, the algorithm requires that the kinetic energy should be low. From the observed and discussed energy variations in Section 2, the kinetic energy is found to be approximately zero throughout the entire folding and deploying processes. The critical moments from one reverse bending tape-spring and two positive bending tape-spring sum to a critical moment of 4592.34 N.mm, and similarly the steady-state moments sum to 320.63 N.mm. The critical moment and steady-state moment of a three tape-spring hinge are not equal to the simple addition of single tape-spring hinges, thus requiring the full physical simulation.

For folding and deploying processes of a three tape-spring hinge, an experimental platform is constructed and utilized to validate the simulation model. Qualitative comparative analysis of experimental and simulation results during deploying processes indicates a good agreement between the predictions. The smooth deployment of the hinge is an important guarantee for the space mission. To ensure the safety performance of the hinge, the maximum von Mises stress of the hinge is obtained at each deployment state.

RSM is used to construct fourth-order models of steady-state moment and maximum von Mises stress as functions of thickness and subtended angle for parameter optimization. Thickness and subtended angle were found to be the two key parameters that have the largest effect on the hinge through parametric analyses. The optimization problem is established with an objective of maximizing steady-state moment and a constraint on maximum stress. The LSGRG algorithm is employed to solve the optimal design problem. Ultimately, an optimal design of $t = 0.132$ mm, $\theta = 86.46^\circ$ is obtained. The optimal responses are 173.94 N.mm and 2000 MPa for steady-state moment and maximum von Mises stress, respectively. Compared with the initial design, the steady-state moment is increased by 19.5%, while stress is held within the allowable range. To verify the effectiveness of the algorithm, the obtained optimal design is modelled and evaluated with the physics-based simulation model. The results of the fitted models seem to differ slightly from the simulation results. Therefore, it is suggested that more than 25 samples points be used to construct the RSM model in order to ensure a higher level of accuracy.

The proposed method does however prove promising in the design of other tape-spring hinges with high stability and low stress values. The results are of great importance in the design of deployable structures.

Acknowledgements This project is supported by the National Natural Science Foundation of China (11072009), Beijing Education Committee Development Project (SQKM201610005001) and Beijing University of Technology Basic Research Fund (001000514313003).

References

- Bourgeois S, Cochelin B, Guinot F, Picault E (2012) Buckling analysis of tape-springs using a rod model with flexible cross-sections. *European Journal of Computational Mechanics/Revue Européenne de Mécanique Numérique* 21(3–6):184–194
- Box GEP, Wilson KB (1951) On the experimental attainment of optimum conditions. *J R Stat Soc* 13(1):1–45
- Dewalque F, Rochus P, Brüls O (2015) Importance of structural damping in the dynamic analysis of compliant deployable structures. *Acta Astronaut.* 111:323–333
- Dewalque F, Collette JP, Brüls O (2016) Mechanical behaviour of tape-springs used in the deployment of reflectors around a solar panel. *Acta Astronaut.* 123:271–282
- Guinot F, Bourgeois S, Cochelin B, Blanchard L (2012) A planar rod model with flexible thin-walled cross-sections. Application to the folding of tape-springs. *Int J Solids Struct* 49(1):73–86
- Guo HW, Zhang J, Liu RQ, Deng ZQ (2013) Effects of joint on dynamics of space deployable structure. *Chinese Journal of Mechanical Engineering* 26(5):861–872
- Hoffait S, Brüls O, Granville D, Cugnon F, Kerschen G (2010) Dynamic analysis of the self-locking phenomenon in tape-spring hinges. *Acta Astronaut.* 66(7–8):1125–1132
- Hou SJ, Dong D, Ren LL, Han X (2012) Multivariable crashworthiness optimization of vehicle body by unreplicated saturated factorial design. *Struct Multidiscip Optim* 46(6):891–905
- Hou SJ, Liu TY, Dong D, Han X (2014) Factor screening and multivariable crashworthiness optimization for vehicle side impact by factorial design. *Struct Multidiscip Optim* 49(1):147–167
- Ju WJ, Yoo YI, Lee JJ, Lim JH, Kim W (2012) Development of a tape spring hinge with a SMA latch for a satellite solar array deployment using the independence axiom. *Ieri Procedia* 1(1):225–231
- Kim KW, Park Y (2015) Systematic design of tape spring hinges for solar array by optimization method considering deployment performances. *Aerosp Sci Technol* 46:124–136
- Li M, Deng ZQ, Liu RQ, Guo HW (2011) Crashworthiness design optimization of metal honeycomb energy absorber used in lunar lander. *Int. J. Crashworthiness* 16(4):411–419
- Li M, Deng ZQ, Guo HW, Liu RQ, Ding BC (2013) Crashworthiness analysis on alternative square honeycomb structure under axial loading. *Chinese Journal of Mechanical Engineering* 26(4):784–792
- Liu YH, Day ML (2008) Bending collapse of thin-walled circular tubes and computational application. *Thin-Walled Struct.* 46(4):442–450
- Mallikarachchi HMYC, Pellegrino S (2011) Quasi-static folding and deployment of ultrathin composite tape-spring hinges. *J Spacecr Rocket* 48(1):187–198
- Mansfield EH (1973) Large-deflection torsion and flexure of initially curved strips. *Proceedings of the Royal Society A Mathematical Physical & Engineering Sciences* 334(1598):279–298
- Qi C, Yang S, Dong FL (2012) Crushing analysis and multiobjective crashworthiness optimization of tapered square tubes under oblique impact loading. *Thin-Walled Struct.* 59:103–119
- Santer M (2010) Actuated bistable jumping structures. *J Appl Mech* 77(3):031009
- Seffen KA (2001) On the behavior of folded tape-springs. *J Appl Mech* 68(3):369–375
- Seffen KA, You Z, Pellegrino S (2000) Folding and deployment of curved tape-springs. *Int J Mech Sci* 42(10):2055–2073
- Sicre J, Givois D (2005) Application of "maeva" hinge to myriade microsatellites deployments needs. *Proceedings of European Space Mechanisms & Tribology Symposium*, 243–250
- Soykasap O (2007) Analysis of tape spring hinges. *Int J Mech Sci* 49(7):853–860
- Soykasap O (2009) Deployment analysis of a self-deployable composite boom. *Compos Struct* 89(3):374–381
- Sui YK, Yu HP (2011) Improvement of response surface method and its application to engineering optimization. Science Press, Beijing (in Chinese)
- Walker SJI, Aglietti GS (2004) Study of the dynamics of three-dimensional tape spring folds. *AIAA J* 42(4):850–856
- Walker SJI, Aglietti GS (2006) Experimental investigation of tape-springs folded in three dimensions. *AIAA J* 44(1):151–159
- Wang Y, Sui SL (2012) Experimental design and MATLAB data analysis. Tsinghua university press, Beijing (in Chinese)
- Wuest W (1954) Einige anwendungen der theorie der zylinderschale. *Journal of Applied Mathematics & Mechanics Zeitschrift Für Angewandte Mathematik Und Mechanik* 34(12):444–454
- Yang H, Deng ZQ, Liu RQ, Wang Y, Guo HW (2014) Optimizing the quasi-static folding and deploying of thin-walled tube flexure hinges

- with double slots. *Chinese Journal of Mechanical Engineering* 27(2):279–286
- Yang H, Liu RQ, Wang Y, Deng ZQ, Guo HW (2015) Experiment and multi-objective optimization design of tape-spring hinges. *Struct Multidiscip Optim* 51(6):1373–1384
- Ye HL, Zhao CH, Zhang Y, Yao Q, Xiao YN (2017) Analysis of mechanical properties in bending processes and optimal design of simple tape spring. *Journal of Modeling in Mechanics and Materials*. <https://doi.org/10.1515/jmmm-2016-0156>
- Yee JC, Pellegrino S (2005) Composite tube hinges. *J Aerosp Eng* 18(4): 224–231
- Yin HF, Fang HB, Xiao YY, Wen GL, Qing QX (2015) Multi-objective robust optimization of foam-filled tapered multi-cell thin-walled structures. *Struct Multidiscip Optim* 52(6):1051–1067